Article:
Gao, J., Jiang, S., Zhang, H. et al. (2021) Facile route to bulk ultrafine-grain steels for high strength and ductility. Nature, 590 (7845). pp. 262-267. ISSN: 0028-0836

https://doi.org/10.1038/s41586-021-03246-3

Facile fabrication of bulk ultrafine-grained high-performance steels via instantaneous nanoprecipitation

Junheng Gao[1], Suihe Jiang[2,*], Huairuo Zhang[3,4*], Yuhe Huang[1], John Nutter[1], Dikai Guan[1], Yidong Xu[1], Shaokang Guan[5], Leonid A. Bendersky[4], Albert V. Davydov[4], Huihui Zhu (Ms)[2], Yandong Wang[2], Zhaoping Lu[2*], W. Mark Rainforth[1*]

[1]Department of Materials Science and Engineering, The University of Sheffield, S1 3JD, UK

[2] Beijing Advanced Innovation Centre for Materials Genome Engineering, State Key Laboratory for Advanced Metals and Materials, University of Science and Technology Beijing, Beijing, 100083, China

[3]Theiss Research, Inc., La Jolla, CA 92037, USA

[4]Materials Science and Engineering Division, National Institute of Standards and Technology (NIST), Gaithersburg, MD 20899, USA

[5]School of Materials Science and Engineering, Zhengzhou University, Zhengzhou, 450002, China

*Corresponding author: huairuo.zhang@nist.gov; jiangsh@ustb.edu.cn; m.rainforth@sheffield.ac.uk; luzp@ustb.edu.cn

Steels with sub-micron grain size usually possess high strength and toughness, which makes them promising candidates for light-weighting technologies and contribute to strategies for energy savings. To date, industrial fabrication of ultrafine-grained alloys are limited to the steels where the microstructure is developed through phase transformation. Here, we report the easy mass production of ultrafine-grained structures in twinning-induced plasticity steels via manipulating the recrystallization process by fast intragranular nanoprecipitation of coherent disordered particles. The rapid and copious nanoprecipitation prevents the growth of freshly recrystallized sub-micro grains, leading to equiaxed ultrafine-grained structures. . Importantly, the precipitates exhibit weak interactions with dislocations and can refine nanotwins, resulting in large uniform ductility of 45% with tensile strengths of 2000 MPa.The current grain refinement concept can be easily extended to other alloy systems, and the manufacturing processes are compatible with existing industrial production lines.

One Sentence Summary: An original economical approach to mass-produce ultrafine grained alloys with superior mechanical properties is developed.

Since Eric O. Hall and Norman J. Petch proposed the well-known Hall-Petch relationship in the 1950s that the yield strength of metallic material scales with the reciprocal square root of grain size (*1, 2*), substantial effort has been devoted to exploring feasible strategies and techniques to achieve the fine structure. Alloys with ultrafine-grained (UFG) structures (less than 1 μm) potentially exhibit a unique combination of high toughness and strength, and are thus highly desirable for enhancing the engineering reliability and energy efficiency. Unfortunately, the broad uses of UFG alloys are still restricted (*3*), although in the past few decades, UFG structures have been achieved by utilizing phase transformation refinement in plain C-Mn steel (*4*),NANOHITEN™ steel (*5, 6*) and the other high-strength low-alloy steels. The main reason is the so-called strength-ductility trade-off phenomenon in these UFG steels, that is, the grain refinement and the accompanied nanoprecipitation of hard carbides results in a substantial increase of strength but at the expense of work hardening and uniform elongation (*3, 7, 8*), which hinders widespread application of these UFG steels (*3*).

For a variety of alloys such as austenitic steels, Cu alloys, Al alloys and high entropy alloys (HEAs), no solid-state phase transformation is available, and the production of UFG structures in these alloys remains in the laboratory. Severe plastic deformation methods such as equal channel angle extrusion, high pressure torsion and nano-grained powder metallurgy are presently mainly utilized for reducing the grain size. These methods are not only costly, but tend to introduce porosity, impurities or a large number of dislocations, which severely deteriorates the plastic deformation capability. More critically, the geometric dimensions of the samples produced is very small, which is a result of the need for ultrahigh strain at low temperature to subdivide the original coarse grains and the subsequent stringent annealing treatment (i.e., very precise control of temperature and time) to prevent the fast coarsening of the fine grains at the annealing temperature (*9, 10*). The rapid coarsening of the fine structure

is due to the high density of grain boundaries that generates a large driving force for grain growth (*11, 12*).

Therefore, to take full advantage of UFG structures and make them more viable for industrial uses, two key challenges have to be addressed. First, the manufacturing process involved should be compatible with existing industrial production lines. As such, the UFG alloys can be fabricated economically in bulk, enabling their commercialization. Second, the stabilization mechanism of UFG structures should not inference with that of plastic deformation so that the strength-ductility trade-off can be reversed. In other words, the conventional grain stabilization strategy such as grain boundary precipitation or segregation of alloying elements at grain boundary is no longer practicable because their preferential distribution at grain boundaries often results in micro-damage at the hetero-interfaces due to the high mechanical mismatch, thus deteriorating mechanical properties (*11, 13*).

Here, we propose a new cost-effective strategy to produce bulk stable UFG structures in the steels with no phase transformation by a simple rolling and annealing process. As an illustration, we refined the microstructure of a typical twinning-induced plasticity (TWIP) steel by inducing a fast intragranular precipitation (within 0.5 min at the beginning of recrystallization) of a type of coherent disordered face-entered cubic (fcc) phase to stabilize the freshly recrystallized matrix, leading to an grain size of 800 ± 400 nm. Contrary to the traditional stabilization strategies of UFG alloys like grain boundary precipitation and segregation, the minimized lattice misfit between the austenite matrix and nanoprecipitates promotes homogeneous precipitation inside the grains during the annealing process. More importantly, these disordered precipitates can be easily cut by dislocations and refine nanotwins, giving rise to the simultaneous increment in the strength and uniform ductility. The current work demonstrates that using fast intragranular precipitation of coherent disordered nanoprecipitates can produce stable and fully dense bulk UFG structures economically, thus

opening a new route for designing high-performance bulk UFG materials.

Due to their unique combination of superior formability, hardenability and high strength, TWIP steels are promising structural materials for lightweight and crash safety in automobile industry, but their performance is currently limited by their low yield strength (*14-16*), which requires the grain sizes below 1 μm. Therefore, we selected a typical Fe-22Mn-0.6C TWIP steel as the demonstration of our approach and studied the Cu-doped alloys, Fe-22Mn-0.6C-xCu (x=0, 1, 2,3,4, and 5, weight per cent, wt %) (*17*). The results show that, when its content exceeds 5 wt %, Cu cannot be fully dissolved into the matrix after solid solution treatment, leading to localized melting and cracking in the steel during rolling, whilst for the alloys with less than 3 % Cu, grain refinement was not evident since the equilibrium fraction of the Cu-rich precipitates is insufficient. Thus, we focused on the study of base alloy, Fe-22Mn-0.6C, and Cu-doped alloys, Fe-22Mn-0.6C-3Cu and Fe-22Mn-0.6C-4Cu, hereafter referred to as 0Cu, 3Cu, and 4Cu alloys, respectively. Fig. 1A shows the true tensile stress-strain curves of the three alloys annealed at 760 ℃ for 5 and 20 min. As can be seen, a significant increase in the yield strength and ultimate tensile strength (σ_{uts}) was observed in the Cu-doped steels. Specifically, the yield strength is nearly doubled from 365 ± 18 MPa for 0Cu alloy to 710 ± 26 MPa for 4Cu alloy after 5 min annealing, whereas the 4Cu alloy retains a comparable ductility with coarse-grained 0Cu alloy (61 ± 5 % engineering strain, Fig. S1). Moreover, the Cu-doped steels exhibit an ultrahigh strain hardening rate (~ 2900 MPa, inset of Fig. 1A), even higher than that (~ 2500 MPa) of 0Cu alloy with micrometre sized grains, which is responsible for the high σ_{uts} (1976 ± 32 MPa) and large uniform elongation. The large uniform elongation of 45 % for 4Cu alloy is highlighted in the normalized strain hardening curve in Fig. 1B, even comparable with that of 0Cu steel. More importantly, an enhanced yield strength (620 ± 21 MPa; Fig. 1A) and large ductility were also observed in the 4Cu alloy annealed at 760 ℃ for 20 min, suggesting the high stability of the Cu-alloyed

microstructure. Yield strength is critical for anti-intrusion beams of vehicles while tensile strength and uniform ductility (both related to work hardening capability) are essential properties responsible for light-weighting, press-forming capability and energy absorption capability for improving crashworthiness during collisions. Thus, we compare yield strength versus the product of σ_{uts} and uniform EL (elongation, EL) of the Cu-alloyed steels in Fig. 1C, with those of other high-performance alloys reported in literature (*14, 18-36*). The Cu-doped TWIP steels and the UFG TWIP steels fabricated by complicated processes, i.e., flash annealing (*36*) or repeated cold rolling and annealing (*26*), exhibit superb combination of high yield strength and exceptionally large values of $\sigma_{uts} \times$ uniform EL (i.e., 71 GPa % for 4Cu alloy), demonstrating that grain refinement is an effective strategy to simultaneously enhance yield strength and toughness. Clearly, the current steels possess a superior dynamic energy absorption capability, a characteristic that is critical for passenger safety in the case of traffic accidents.

Fig. 2 A and B display the synchrotron high-energy X-ray diffraction (XRD) pattern and electron back-scattering diffraction (EBSD) map of the 4Cu alloy annealed at 760 ℃ for 5 min, respectively, revealing a single-phase fully recrystallized fcc structure with a fine grain size of 800 ± 400 nm. Further analysis with annular dark-field scanning transmission electron microscopy (ADF-STEM) in Fig. 2C revealed the presence of nanoprecipitates (bright particles) with a high number density and uniform intragranular distribution. The energy-dispersive spectroscopy spectrum-imaging (EDS-SI) image (inset of Fig. 2C) from the marked region of the grains with a relatively bright contrast confirms the homogeneous distribution of intragranular nanoprecipitates which are enriched in Cu. The selected area electron diffraction pattern (Fig. S2) taken along the $[110]_{fcc}$ zone axis does not show any additional reflections to the fcc matrix. Analysis of the atomic resolution high angle ADF-STEM (HAADF-STEM) () image shows that the precipitate in bright contrast does not exhibit extra periodicity to the fcc

matrix, confirming its disordered fcc nature. Moreover, these precipitates with a diffuse interface are fully coherent with the matrix (Fig. 2D), which is responsible for their homogeneous nucleation (*37*). Note that under the same thermomechanical treatment (Fig. S3), a UFG structure (900 $\pm$ 400 nm) was also obtained in 3Cu alloy along with formation of high-density Cu-rich particles, whilst the grain size of 0Cu steels reaches 2.2 $\pm$ 1.1 μm.

Atom probe tomography (APT) was further used to characterize the characteristics of the Cu-rich nanoprecipitates and elemental distribution around grain boundaries. The reconstruction data in Fig. 2E confirms that Cu-rich nanoprecipitates with a high number density of about 4.6×10^{23} m^{-3} and a small diameter of 5.6 ± 2.5 nm are uniformly distributed inside grains, whilst a precipitate free zone (~ 50 nm in width) adjacent to the grain boundaries in coarser grains was observed. The proximity histograms in Fig. 2F reveal that the Cu content is 84 ± 6 at %. The 1D concentration profiles (Fig. 2G and Fig. S4) of cylindrical regions across grain boundaries demonstrate that, except for slight C segregation (*38*), no Cu and Mn segregation at grain boundaries occurred. Therefore, different from the conventional stabilization strategies (e.g., boundary segregation and precipitation), the current approach did not introduce any crystallographic defects (e.g., hard precipitates, segregation at grain boundaries, unrecovered dislocations, etc.), which is certainly beneficial for plastic deformation.

Since the thermal stability of UFG alloys determines the processing window of manufacturing, e.g., the width of annealing temperature and time, and is also critical for high-temperature service (*12*), we evaluated the thermal stability of 0Cu alloy, UFG 3Cu and 4Cu alloys over a wide annealing temperature span (760 to 910 ℃) and time range (5 to 60 min) (Fig. 3 and Figs. S5 and S6). The 0Cu alloy exhibited a stronger tendency for grain growth with annealing temperature. In contrast, 4Cu alloy exhibited a very stable structure, even when the annealing temperature reaches up to 910 ℃ (Fig. 3A and Fig. S5), that is 0.64 T_m of 4Cu

alloy (for 4Cu alloy, T_m, the melting point, is about 1430 ℃), demonstrating a broad temperature processing window of 150 ℃. Although the 3Cu alloy is stable from 760 to 860 ℃ with an only slight increase in grain size from 0.9 to 1.4 μm, nevertheless, grain growth is rather quick at 910 ℃ (Fig. 3B and Fig. S5). Furthermore, with an extension of annealing time from 5 to 60 min at 760 ℃, limited grain growth was observed in 4Cu alloy (i.e., from 0.8 to 1.3 μm) whereas for the 0Cu alloy, grains grow more significantly from 2.1 to 5.7 μm (Fig. 3B and Fig. S6). Hence, owing to the enhanced thermal stability, UFG structures in the current TWIP steels can be obtained in a wide range of annealing temperature and time, which is important for the mass-production of UFG alloys. The desirable thermal stability is attributed to the continued pinning effect of highly dispersed Cu-rich nanoprecipitates, as discussed below, which is profoundly distinguished from other UFG alloys, such as low carbon steel (*39*), Al alloys (*40*) and Ti (*41*), where rapid grain growth occurred when the annealing temperature approaches 0.3Tm.

To uncover the underlying mechanism responsible for the formation of such desirable UFG structures, we studied the integrated recrystallization and precipitation process. The 4Cu alloy annealed at 760 ℃ for 0.5, 1 and 2 min was investigated using EBSD, annular bright-field (ABF) STEM and APT analysis (Fig. 4 A and B and Figs. S7 and S8). The analyses show that after 0.5 min annealing, nucleation of recrystallization occurred extensively and Cu-rich clusters with an average diameter of 2.6 nm and a high number density of 1.6×10^{24} m^{-3} were formed (Fig. 4A and Fig. S7A), confirming the rapid and homogenous precipitation at the onset of recrystallization. When the annealing time was prolonged to 1 min, equiaxed grains with a size of 300 ± 150 nm was observed (Fig. S8A) and 76 % volume fraction of the deformed matrix has recrystallized (Fig. S7B). The average precipitate size of the Cu-rich clusters increases to 3.7 nm while the number density decreases slightly to 8.8×10^{23} m^{-3} (Fig. S8B). As the annealing time is further extended to 2 min, the size of equiaxed grain increases to 500

± 200 nm with ~ 95 % volume fraction recrystallized (Fig. 4B and Fig. S7C). The average size of Cu-rich precipitate increases slightly to 4.5 nm while the number density decreases to 6.1 × 10^{23} m^{-3} (Fig. 4B). More interestingly, accompanying with the size growth, the Cu content in these precipitates also increases from 56 ± 4 to 76 ± 5 at %, as shown by the proximity histograms in Fig. 4 A and B, respectively. To exclude the effect of trajectory aberrations on the composition of small particles, we corrected the compositions using the methods proposed by Blavette et al. (*42*) (Fig. S9). The enrichment of Cu in the precipitates with growth suggests that the formation of these disordered precipitates is dominated by a simple solute-enrichment process, which should contribute to the rapid precipitation as discussed below. Obviously, both recrystallization and precipitation start immediately after annealing and both processes proceed rapidly. As a result, the Cu-rich clusters quickly developed into high-density precipitates right at the onset of grain growth, thus effectively and timely stabilizing the freshly recrystallized submicron grains from further growth.

We then evaluated the interrelationship between recrystallization and precipitation and the mechanism responsible for the long-term stability of 4Cu alloy by comparing the evolution of the driving pressure for recrystallization (P_r), Zener pinning pressure (P_z), and driving pressure for grain growth (P_g) as a function of annealing time at 760 ℃ (Fig. 4C). P_r is the stored energy during cold rolling, which decreases rapidly from 28.6 to 3.3 MPa after 2 min annealing (95 % recrystallized). Note that since the dislocation density is an averaged result between deformed grains and recrystallized grains, the local dislocation density of the un-recrystallized grains actually decreases slightly. Thus, the driving energy for the deformed matrix to recrystallize should stay constant, a value which is much higher than P_z offered by the precipitates, leading to full recrystallization of the deformed microstructure after ~ 2-3 min annealing. However, due to the rapid and copious precipitation at the onset of annealing, the P_z increases rapidly and immediately exceeds P_g (the pressure difference between each side of

one grain boundary due to grain boundary curvature (*43*)) after 1 min annealing, suggesting that these freshly recrystallized submicron grains were stabilized right after recrystallization. When the annealing extends from 1 to 5 min, the precipitates grow slightly from 3.7 to 5.6 nm, and P_z peaks at around 5 min (Fig. 4C), whilst P_g decreases gradually. When the annealing time exceeds 5 min, nanoprecipitation develops into the capillary-driving coarsening stage which generally exhibits very slow kinetics due to the low driving force and long-range diffusion character. As a result, P_z is inevitably decreased but still higher than P_g due to the high-density nanoprecipitates, indicating that the UFG structure is continuously stabilized by Zener pinning (Fig. 4 D and E).

It should be noted that the pinning effect actually stems from the precipitates adjacent to grain boundaries (Fig.4 D and E). However, the coarsening of the precipitates would unavoidably decrease the number of precipitates near grain boundaries and increase the space between these precipitates and the boundaries. As the grain boundaries of the submicron grains are highly mobile, they would quickly migrate towards these precipitate-free regions (where Zener pinning effect becomes absent) until they interact with new precipitates. As can be seen in Fig. 4 D and E, migration of the grain boundary, which closely contacts with the encountered precipitates in the shrinking grains, is therefore dependent on the coarsening of precipitates. Such a local growth process leaves a precipitate-free space behind with a width of ~ 50 nm in the coarsened grains (Fig. 2E and Fig. 4D). In general, grain growth is a short-range interface process, i.e., migration of the boundary does not need long-range diffusion of the constituents, yet a relatively fast process as shown in many pure UFG alloys (*44*). Once the boundaries are pinned by nanoprecipitates, coarsening of the nanoprecipitates, which actually is a much slower long-range diffusion process (*45*), then governs the grain growth process as the coarsening of nanoprecipitates increases the interspace between precipitates and grain boundaries and leads to subsequent grain growth. In conjunction with the low-misfit, fully coherent interfaces which

minimize the driving force for precipitate coarsening, the intrinsically unstable UFG grains are then stabilized by the nanoprecipitates. In fact, the average grain size slowly increases from 0.8, 1.2 to 1.3 μm in 4Cu alloy with an extension of annealing time from 5, 20 to 60 min (Fig. 3B and Figs. S5 and S6). Fig. 4F shows the high-resolution TEM (HRTEM) image of the nanoprecipitate marked in Fig. 4E, which is coherent with the shrinking grain, clearly confirming that the continuous strong Zener pinning effect is resulted from the intragranular nanoprecipitates, instead of grain boundary precipitation.

The above results vividly manifest the importance of the rapid and copious intragranular nanoprecipitation on stabilization of the freshly recrystallized grains and the continuous stabilization of the resulting UFG structure. The reasons for the rapid and copious precipitation are threefold. One is the fast kinetics resulting from higher annealing temperature, as compared with that of other high-Mn steels (*46*) (typical around 550 ℃ and ageing durations around 20 hours). The second is the minimized nucleation barrier resulting from the coherent interfaces (*37*) and the shorter incubation time due to the disordered nature. The disordered nature of Cu-rich precipitates renders the precipitation just a continuous Cu localized enrichment process (Fig. 4 A and B), which greatly reduces the incubation time in comparison with that of intermetallic precipitates that require localized enrichment of at least two elements with a strict stoichiometric ratio. Thirdly, the positive mixing enthalpy between Cu and Fe (13 kJ/mol) (*47*) suggests that atomic scale Cu-rich clusters would exist in the melt, which also facilitates fast precipitation. Moreover, the fully coherent interface also yields a low interfacial energy of Cu-rich nanoprecipitates in the austenite matrix of about 17 mJ/m^2 (*48*), which is the driving energy for precipitates coarsening, thus preventing these nanoprecipitates from rapid coarsening at high temperatures (*37*), and hence maintaining a continuously high P_Z.

Compared with the 0Cu alloy annealed at 760 ℃ for 5 min (Fig. 1A), the total increment of yield strength for the 4Cu alloy is 345 MPa, which is attributed to the synergistic effects of

grain refinement, solid solution strengthening of Cu and precipitation strengthening. According to the calculation (*17*), the grain refinement dominates the yield strength enhancement, and its contribution was estimated to be 286 MPa. Owing to the ultralow elastic misfit (the lattice misfit is only 0.11 %) and the disordered nature, the elastic and interfacial strengthening of the Cu-rich nanoprecipitates were estimated to be 19.9 and 0.08 MPa respectively (*17*). Therefore, the main role of these coherent Cu-rich precipitates is to refine the grain size, distinguishing them from other hard nanoprecipitates in maraging steels (*37*) and HSLA steels (*5*) which were introduced mainly for strengthening.

To uncover the role of Cu-rich nanoprecipitates in dislocation motion and nanotwin formation, we fabricate a UFG 0Cu alloy with a grain size of 1.1 ± 0.5 μm (Fig. S10) by a special two-step cold rolling and flash annealing process to minimize the effect of grain size for comparison. We analysed the microstructure and calculated the respective hardening contribution (Fig. S11) from dislocations and nanotwins of 4Cu and UFG 0Cu alloys at the tensile strain of 15 % and 45 %, respectively. In the early deformation stage (i.e., ≤ 15 % strain), a high density of dislocation walls and cells were observed in both alloys (Fig. 5 A and B), along with some nanotwins with interspacing of 300-500 nm. The dislocation density of 4Cu and UFG 0Cu alloys was estimated to be 3.5×10^{15} and 3.9×10^{15} m^{-2}, respectively (Fig. S12). It seems that dislocations dominate strain hardening for both steels during this stage, and the Cu-rich nanoprecipitates exhibit a negligible effect due to its small strengthening contribution.

A further increase of strain to 45 % leads to continuous formation of nanotwins in both UFG alloys (Fig. 5 C and D and Fig. S13). The average width and interspacing of the nanotwins in 4Cu alloy are 7.9 ± 5.4 and 15.2 ± 14.3 nm, respectively, whilst those in UFG 0Cu alloy are much larger, i.e., 15.6 ± 13.7 and 69.2 ± 38.4 nm, respectively. Due to the thinner and denser distribution of twins beyond 15 % strain, twinning gradually dominates the strain

hardening in 4Cu alloy, whereas dislocations still govern hardening in the UFG 0Cu steel (Fig. S11), which is consistent with conventional TWIP steels without precipitates (*49*).

At the early plastic deformation stage, part of the Cu-rich particles was sheared through by dislocations and obviously flattened along the loading direction (Fig. 5E and Fig. S14), which is consistent with their weak strengthening effect. At the late stage, the Cu-rich precipitates were uniformly fragmented into smaller ones (Fig. 5F), leading to a much increased number density. The STEM EDS-SI images in Fig. 5 G and H confirm that the nanotwins frequently cut through the Cu-rich precipitates and in combination with dislocation shearing, caused the fragmentation, and in return, the Cu-rich clusters refined nanotwins, leading to the twining-dominant deformation at this stage. Different from full dislocation movement, twinning proceeds via co-operative motion of Shockley partials on the subsequent {111} plane. When the partial dislocations cut through the Cu-rich clusters, a stacking fault with higher energy in the Cu-rich clusters (78 mJ/m^2 for Cu-rich precipitates (*50*) and 22 mJ/m^2 for matrix (*16*) would emerge as an additional obstacle to resist subsequent twining and constrained the growth of the twins, thus refining twining substructures. More importantly, numerous small dislocation cells were observed around the thinner and denser nanotwins (Fig. S15), suggesting that the refined nanotwins could still accommodate additional dislocation accumulation, which is also critical for sustaining a continuous high strain hardening rate. In brief, the Cu-rich nanoprecipitates can be sheared by dislocations, thus relaxing the local stress concentration around these nanoprecipitates. Furthermore, the difference in stacking fault energy causes a refined nanotwin substructure, thereby resulting in stronger dynamic strengthening and large uniform ductility.

To clarify the universality of the proposed approach, we have summarized the alloy design principle and selection criterion of the strategic element (i.e., Cu in this study) in Materials and Methods (i.e., Composition design), which could extend our approach to a wide

range of alloy systems. For demonstration, we also added 3Cu wt % into a typical Fe-Mn-C TRIP steel (*51*) and Co-Cr-Ni medium-entropy alloy (*52*) and adopted the similar thermomechanical process route in this work. As shown in Figs. S16 and S17, UFG structures with greatly enhanced mechanical properties were obtained, further confirming the validity and applicability of our approach. Thus, our grain refinement concept may lead to the developments of a series of UFG alloys with superior mechanical performances by simple rolling and annealing process, which is of great significance for the industrial production and broad usage of UFG alloys, particularly for alloys without phase transformation refinement.

REFERENCES AND NOTES

1. E. Hall, The deformation and ageing of mild steel: III discussion of results. *Proc. Phys. Soc.,B* **64**, 747 (1951).
2. N. Petch, The cleavage strength of polycrystals. *J. Iron Steel Inst.* **174**, 25-28 (1953).
3. A. Howe, Ultrafine grained steels: industrial prospects. *Mater. Sci. Technol.* **16**, 1264-1266 (2000).
4. R. Song, D. Ponge, D. Raabe, J. G. Speer, D. K. Matlock, Overview of processing, microstructure and mechanical properties of ultrafine grained bcc steels. *Mater. Sci. Eng. A* **441**, 1-17 (2006).
5. K. Seto, Y. Funakawa, S. Kaneko, "Hot rolled high strength steels for suspension and chassis parts “NANOHITEN” and “BHT® Steel”," JFE Tech. Rep. No.10 (2007).
6. Y. Funakawa, T. Shiozaki, K. Tomita, T. Yamamoto, E. Maeda, Development of high strength hot-rolled sheet steel consisting of ferrite and nanometer-sized carbides. *ISIJ Int.* **44**, 1945-1951 (2004).
7. R. Song, D. Ponge, D. Raabe, Mechanical properties of an ultrafine grained C–Mn steel processed by warm deformation and annealing. *Acta Mater.* **53**, 4881-4892 (2005).
8. A. Ohmori, S. Torizuka, K. Nagai, Strain-hardening due to dispersed cementite for low carbon ultrafine-grained steels. *ISIJ Int.* **44**, 1063-1071 (2004).

9. M. Dao, L. Lu, R. J. Asaro, J. T. M. De Hosson, E. Ma, Toward a quantitative understanding of mechanical behavior of nanocrystalline metals. *Acta Mater.* **55**, 4041-4065 (2007).

10. R. Valiev, Nanostructuring of metals by severe plastic deformation for advanced properties. *Nature Mater.* **3**, 511-516 (2004).

11. X. Zhou, X. Y. Li, K. Lu, Enhanced thermal stability of nanograined metals below a critical grain size. *Science* **360**, 526-530 (2018).

12. T. Chookajorn, H. A. Murdoch, C. A. Schuh, Design of stable nanocrystalline alloys. *Science* **337**, 951-954 (2012).

13. M. A. Gibson, C. A. Schuh, Segregation-induced changes in grain boundary cohesion and embrittlement in binary alloys. *Acta Mater.* **95**, 145-155 (2015).

14. O. Bouaziz, H. Zurob, M. Huang, Driving Force and Logic of Development of Advanced High Strength Steels for Automotive Applications. *Steel Res. Int.* **84**, 937-947 (2013).

15. O. Bouaziz, S. Allain, C. Scott, P. Cugy, D. Barbier, High manganese austenitic twinning induced plasticity steels: A review of the microstructure properties relationships. *Curr. Opin. Solid State Mater. Sci.* **15**, 141-168 (2011).

16. B. C. De Cooman, Y. Estrin, S. K. Kim, Twinning-induced plasticity (TWIP) steels. *Acta Mater.* **142**, 283-362 (2018).

17. Materials and methods including composition desgin are available as supplementary materials.

18. Z. Chen, H. J. Bong, D. Li, R. Wagoner, The elastic–plastic transition of metals. *Int. J. Plast.* **83**, 178-201 (2016).

19. O. Grässel, L. Krüger, G. Frommeyer, L. W. Meyer, High strength Fe–Mn–(Al, Si) TRIP/TWIP steels development — properties — application. *Int. J. Plast.* **16**, 1391-1409 (2000).

20. J.-l. Zhao, Y. Xi, W. Shi, L. Li, Microstructure and Mechanical Properties of High Manganese TRIP Steel. *J. Iron Steel Res. Int.* **19**, 57-62 (2012).

21. M. Zhang, L. Li, R. Y. Fu, D. Krizan, B. C. De Cooman, Continuous cooling transformation diagrams and properties of micro-alloyed TRIP steels. *Mater. Sci. Eng. A* **438-440**, 296-299 (2006).

22. X. Gu, Y. Xu, F. Peng, R. D. K. Misra, Y. Wang, Role of martensite/austenite constituents in novel ultra-high strength TRIP-assisted steels subjected to non-isothermal annealing. *Mater. Sci. Eng. A* **754**, 318-329 (2019).

23. J. N. Huang *et al.*, Combining a novel cyclic pre-quenching and two-stage heat treatment in a low-alloyed TRIP-aided steel to significantly enhance mechanical properties through microstructural refinement. *Mater. Sci. Eng. A* **764**, 138231 (2019).

24. E. De Moor, J. G. Speer, D. K. Matlock, J.H. Kwak, S.-B. Lee, Effect of carbon and manganese on the quenching and partitioning response of CMnSi steels. *ISIJ Int.* **51**, 137-144 (2011).

25. H. Gwon, J.-K. Kim, S. Shin, L. Cho, B. C. De Cooman, The effect of vanadium micro-alloying on the microstructure and the tensile behavior of TWIP steel. *Mater. Sci. Eng. A* **696**, 416-428 (2017).

26. Y. Tian *et al.*, A novel ultrafine-grained Fe22Mn0. 6C TWIP steel with superior strength and ductility. *Materials Charact.* **126**, 74-80 (2017).

27. G. Dini, A. Najafizadeh, R. Ueji, S. M. Monir-Vaghefi, Improved tensile properties of partially recrystallized submicron grained TWIP steel. *Materials Lett.* **64**, 15-18 (2010).

28. Y. W. Kim, J. H. Kim, S.-G. Hong, C. S. Lee, Effects of rolling temperature on the microstructure and mechanical properties of Ti–Mo microalloyed hot-rolled high strength steel. *Mater. Sci. Eng. A* **605**, 244-252 (2014).

29. A. Arlazarov, O. Bouaziz, A. Hazotte, M. Gouné, S. Allain, Characterization and modeling of manganese effect on strength and strain hardening of martensitic carbon steels. *ISIJ Int.* **53**, 1076-1080 (2013).

30. D. Zhang *et al.*, Additive manufacturing of ultrafine-grained high-strength titanium alloys. *Nature* **576**, 91-95 (2019).

31. I. Sabirov, M. Y. Murashkin, R. Valiev, Nanostructured aluminium alloys produced by severe plastic deformation: New horizons in development. *Mater. Sci. Eng. A* **560**, 1-24 (2013).
32. S.-H. Kim, H. Kim, N. J. Kim, Brittle intermetallic compound makes ultrastrong low-density steel with large ductility. *Nature* **518**, 77 (2015).
33. H. L. Chan, H. H. Ruan, A. Y. Chen, J. Lu, Optimization of the strain rate to achieve exceptional mechanical properties of 304 stainless steel using high speed ultrasonic surface mechanical attrition treatment. *Acta Mater.* **58**, 5086-5096 (2010).
34. P. Zhou, Z. Liang, R. Liu, M. Huang, Evolution of dislocations and twins in a strong and ductile nanotwinned steel. *Acta Mater.* **111**, 96-107 (2016).
35. S. S. Sohn *et al.*, Ultrastrong Medium‐Entropy Single‐Phase Alloys Designed via Severe Lattice Distortion. *Advanced Mater.* **31**, 1807142 (2019).
36. K. M. Rahman, V. A. Vorontsov, D. Dye, The effect of grain size on the twin initiation stress in a TWIP steel. *Acta Mater.* **89**, 247-257 (2015).
37. S. Jiang *et al.*, Ultrastrong steel via minimal lattice misfit and high-density nanoprecipitation. *Nature* **544**, 460 (2017).
38. D. Blavette, E. Cadel, A. Fraczkiewicz, A. Menand, Three-dimensional atomic-scale imaging of impurity segregation to line defects. *Science* **286**, 2317-2319 (1999).
39. K.-T. Park, Y.-S. Kim, J. G. Lee, D. H. Shin, Thermal stability and mechanical properties of ultrafine grained low carbon steel. *Mater. Sci. Eng. A* **293**, 165-172 (2000).
40. H. Hasegawa *et al.*, Thermal stability of ultrafine-grained aluminum in the presence of Mg and Zr additions. *Mater. Sci. Eng. A* **265**, 188-196 (1999).
41. M. Hoseini *et al.*, Thermal stability and annealing behaviour of ultrafine grained commercially pure titanium. *Mater. Sci. Eng. A* **532**, 58-63 (2012).
42. D. Blavette, P. Duval, L. Letellier, M. Guttmann, Atomic-scale APFIM and TEM investigation of grain boundary microchemistry in Astroloy nickel base superalloys. *Acta Mater.* **44**, 4995-5005 (1996).

43. F. J. Humphreys, M. Hatherly, "[Recovery after defromaiton]" in *Recrystallization and Related Annealing Phenomena* (Elsevier, Amsterdam; Boston, ed.2, 2004), pp. 169-213 (Elsevier, 2012).

44. J. Lian, R. Z. Valiev, B. Baudelet, On the enhanced grain growth in ultrafine grained metals. *Acta Metall. Mater.* **43**, 4165-4170 (1995).

45. D. Fan, L.-Q. Chen, Diffusion-controlled grain growth in two-phase solids. *Acta mater.* **45**, 3297-3310 (1997).

46. M. J. Yao *et al.*, Strengthening and strain hardening mechanisms in a precipitation-hardened high-Mn lightweight steel. *Acta Mater.* **140**, 258-273 (2017).

47. A. Takeuchi, A. Inoue, Classification of bulk metallic glasses by atomic size difference, heat of mixing and period of constituent elements and its application to characterization of the main alloying element. *Materials Trans.* **46**, 2817-2829 (2005).

48. J. W. Bai *et al.*, Coherent precipitation of copper in Super304H austenite steel. *Mater. Sci. Eng. A* **584**, 57-62 (2013).

49. Z. Y. Liang, Y. Z. Li, M. X. Huang, The respective hardening contributions of dislocations and twins to the flow stress of a twinning-induced plasticity steel. *Scripta Mater.* **112**, 28-31 (2016).

50. L. E. Murr, Interfacial phenomena in metals and alloys. (Addison Wesley, Reading, MA, 1975).

51. J. H. Choi *et al.*, Cu addition effects on TRIP to TWIP transition and tensile property improvement of ultra-high-strength austenitic high-Mn steels. *Acta Mater.* **166**, 246-260 (2019).

52. R. Zhang *et al.*, Short-range order and its impact on the CrCoNi medium-entropy alloy. *Nature* **581**, 283-287 (2020).

ACKNOWLEDGMENTS

Funding: We thank J. Nutter (University of Sheffield) for technical assistance with precession electron diffraction characterization. J.H.G. and W.M.R. would like to acknowledge EPSRC project "Designing Alloys for Resource Efficiency (DARE)" (EP/L025213/1) for the financial support, and the Henry Royce Institute for Advanced Materials (EP/R00661X/1) for JEOL F200 Transmission Electron Microscope access at Royce @ Sheffield. Z.P.L. and S.H.J. acknowledges financial support from the National Natural Science Foundation of China (Nos. 51531001, 51921001, 51671018, 51971018 and 11790293), 111 Project (B07003) and Innovative Research Team in University (IRT_14R05), the Projects of SKL-AMM-USTB (2018Z-01, 2018Z-19 & 2019Z-01), the Fundamental Research Fund for the Central Universities of China (FRF-TP-18-093A1) and National Postdoctoral Program for Innovative Talents (BX20180035). H.Z. acknowledges support from the U.S. Department of Commerce, NIST under the financial assistance awards 70NANB17H249 and 70NANB19H138. A.V.D. acknowledges support from Materials Genome Initiative funding allocated to NIST. **Author contributions:** J.H.G conceived the idea. J.H.G, S.H. J., W.M.R. and Z. P. L. designed the experimental program. J.H.G carried out the main experiments. S.H.J. and Z.P.L. conducted the 3D-APT, Synchrotron experiment and analysed the data. H.R.Z. conducted the HR-STEM characterization and analysed the data. J.H.G. and H.R.Z. conducted STEM-EDS mapping. Y.H.H. analysed XRD patterns for calculation of dislocation density. J.H.G., S.H.J., H.R.Z., Z.P.L. and W.M.R wrote the manuscript and discussed the results. All authors reviewed and contributed to the final manuscript. **Competing interests:** The authors declare no complicit of interest. **Data and materials availability:** All data is available in the main text or the supplementary materials.

SUPPLEMENTARY MATERIALS

Materials and methods

Figs. S1 to S17

Table S1

References (53-60)

Fig.1

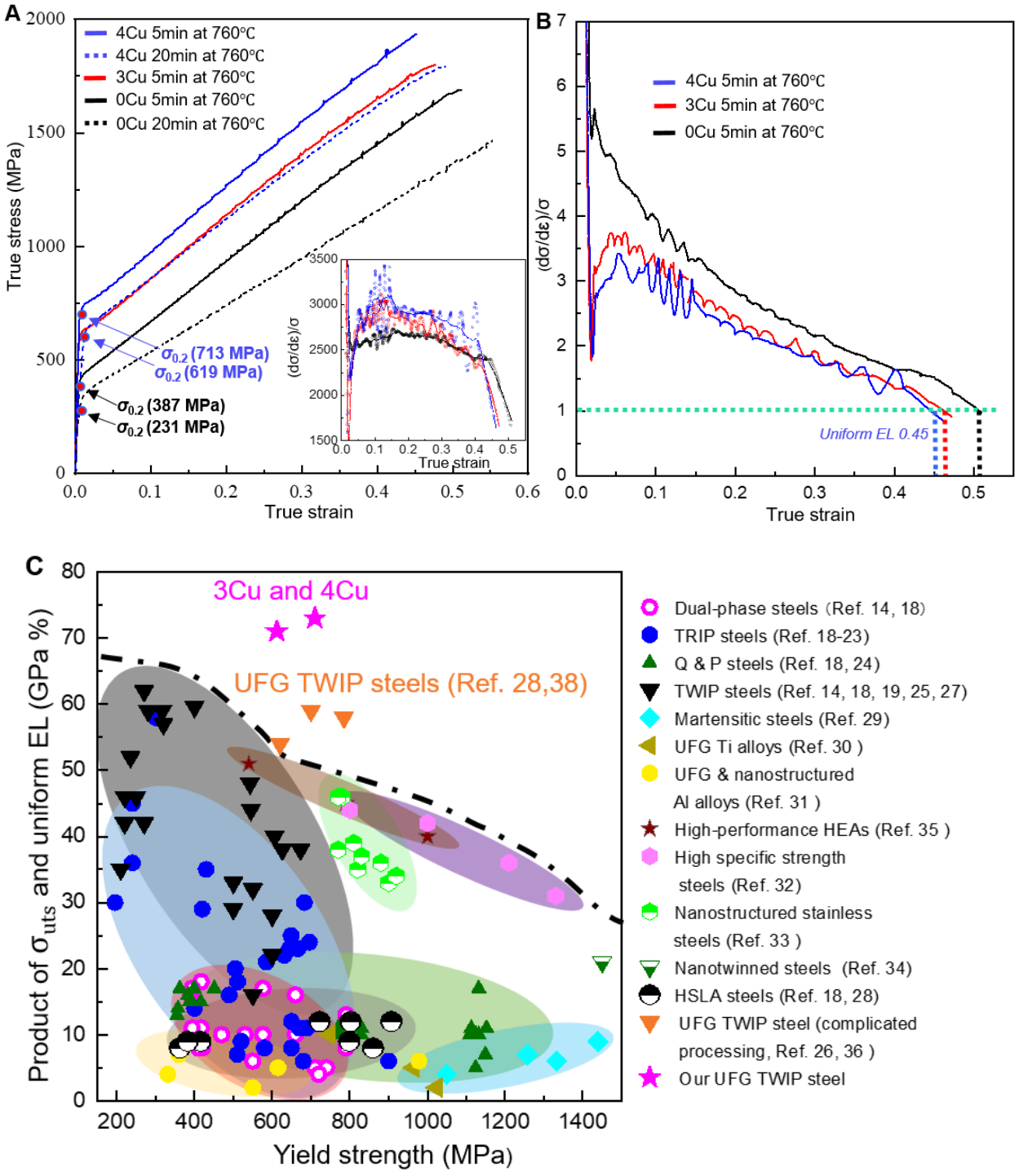

Figure 1. Mechanical properties. (**A**), Room-temperature tensile stress-strain curves of 0Cu, 3Cu and 4Cu alloys annealed for 5 and 20 min at 760 ℃. A significant increase of strength without sacrifice of ductility was achieved in the Cu-doped steels. The inset is the corresponding strain hardening response (dσ/dε) of 0Cu, 3Cu and 4Cu alloys annealed for 5

min at 760℃. Higher work hardening rates were observed for the Cu-doped steels. (**B**), Normalized strain hardening response ((dσ/dε)/σ) showing a large uniform elongation of 45 % true strain for 4Cu alloy. (**C**), Yield strength versus the product of σ_{uts} and uniform EL of 3Cu and 4Cu alloys, as compared with those of other high performance materials reported in literature (*14, 18-36*). The Cu-doped steels and the UFG TWIP steels fabricated by flash annealing or repeatedly cold rolling and annealing have exceptionally high values of σ_{uts} × uniform EL, suggesting a superior combination of strength and ductility.

Fig.2

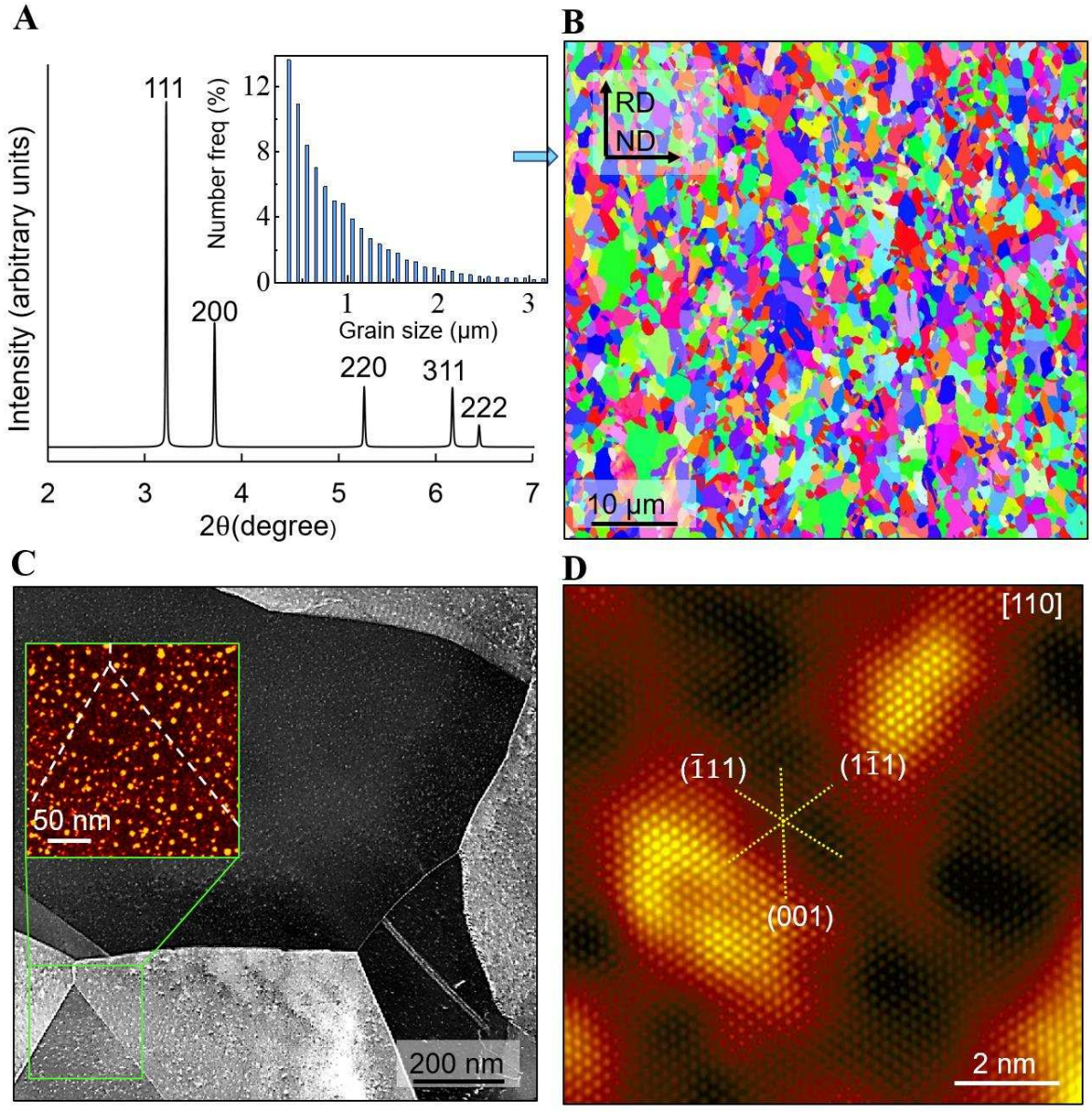

Fig.2 (continue)

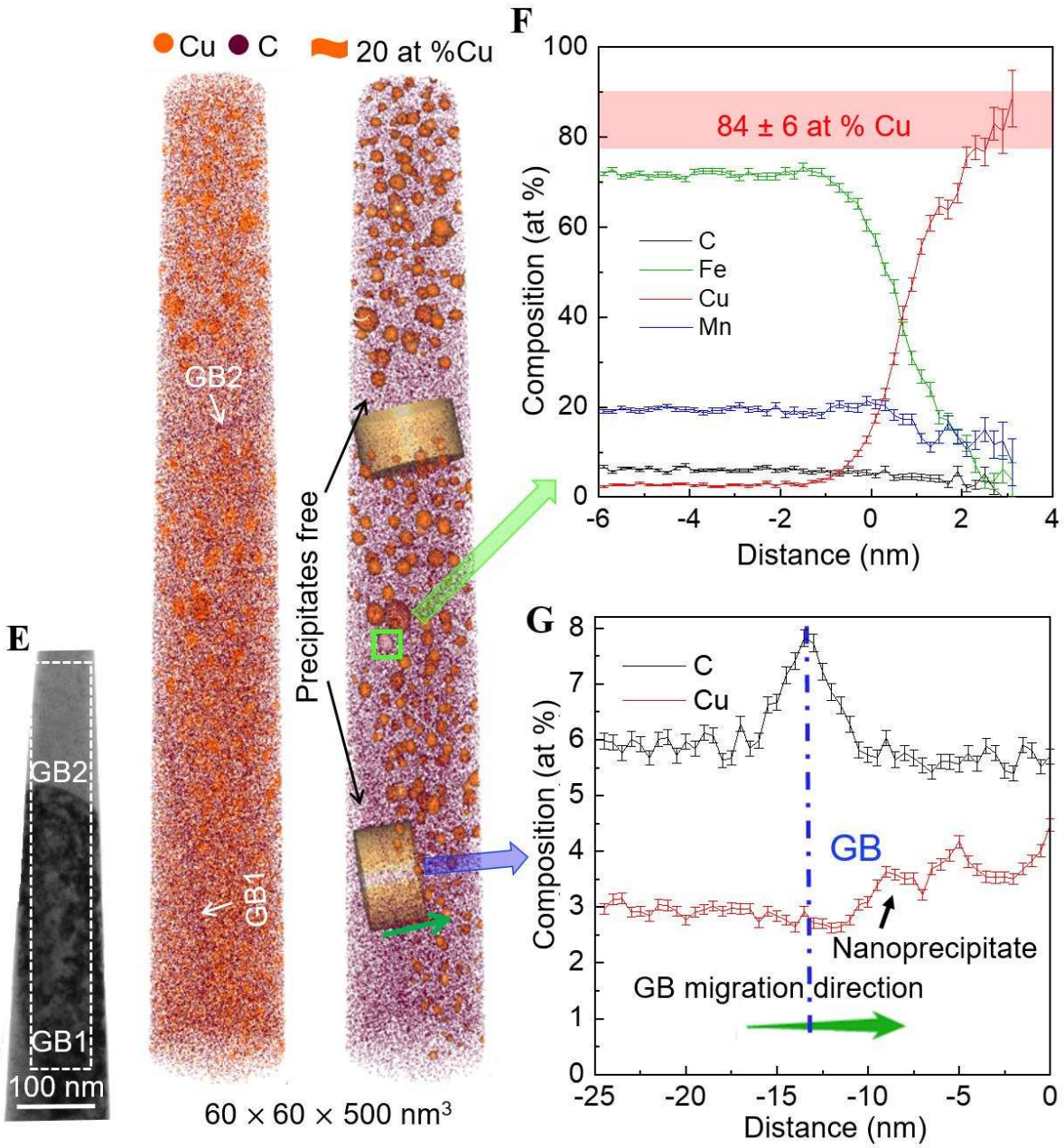

Figure 2 Microstructure characterization of 4Cu alloy annealed at 760 ℃ for 5 min. (**A**), (**B**), Synchrotron high-energy XRD pattern and EBSD map showing a single fcc structure with a grain size of 800 ± 400 nm. The inset in (**A**) is the grain size distribution. (**C**), ADF-STEM image displaying a typical ultrafine structure with a high density of intragranular nanoprecipitates (bright particles). The inset is the STEM EDS-SI image demonstrating that the nanoprecipitates are enriched in Cu and homogeneously distributed inside grains. (**D**),

Atomic resolution HAADF-STEM image showing that the bright Cu-rich nanoprecipitates are fully coherent with the matrix and do not exhibit extra periodicity to fcc matrix (disordered nature). (**E**), Correlated TEM and atom probe analysis across two grain boundaries presenting the size, morphology and spatial distribution of Cu-rich nanoprecipitates. **f,** Proximity histogram across one nanoprecipitate (marked by the green square in (E)) . **g,** 1D concentration profile of cylindrical region across one grain boundary (i.e., GB1) demonstrating that, except for slight C segregation, no Cu and Mn segregation at grain boundary. The error bars are standard deviations of the mean while the isoconcentration surface is 20 at % Cu.

Fig.3

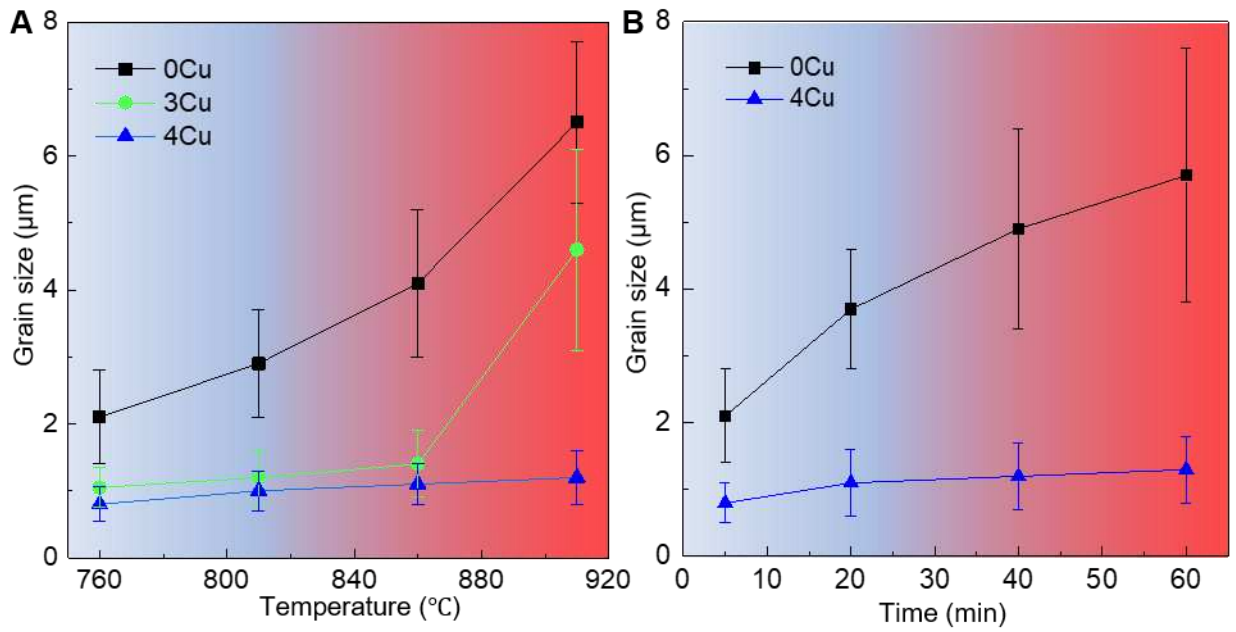

Figure 3 Effects of annealing temperature and time on the UFG structure. (**A**), Evolution of grain size of 0Cu, 3Cu and 4Cu alloys after annealing at 760, 810, 860 and 910 ℃ for 5 min. Rapid grain growth was observed for 0Cu alloy with the increase of annealing temperature, whilst 4Cu alloy exhibits the most stable UFG structure between 760 and 910 ℃.(**B**), Evolution of grain size of 0Cu and 4Cu alloys as a function of annealing time at 760 ℃, showing that with extension of annealing time from 5 to 60 min, the grain size of 4Cu increases slightly from 0.8 to 1.3 μm, whereas the grains of 0Cu alloy coarsened rapidly from 2.1 to 5.7 μm. The error bars are standard deviations of the mean.

1 **Fig.4**

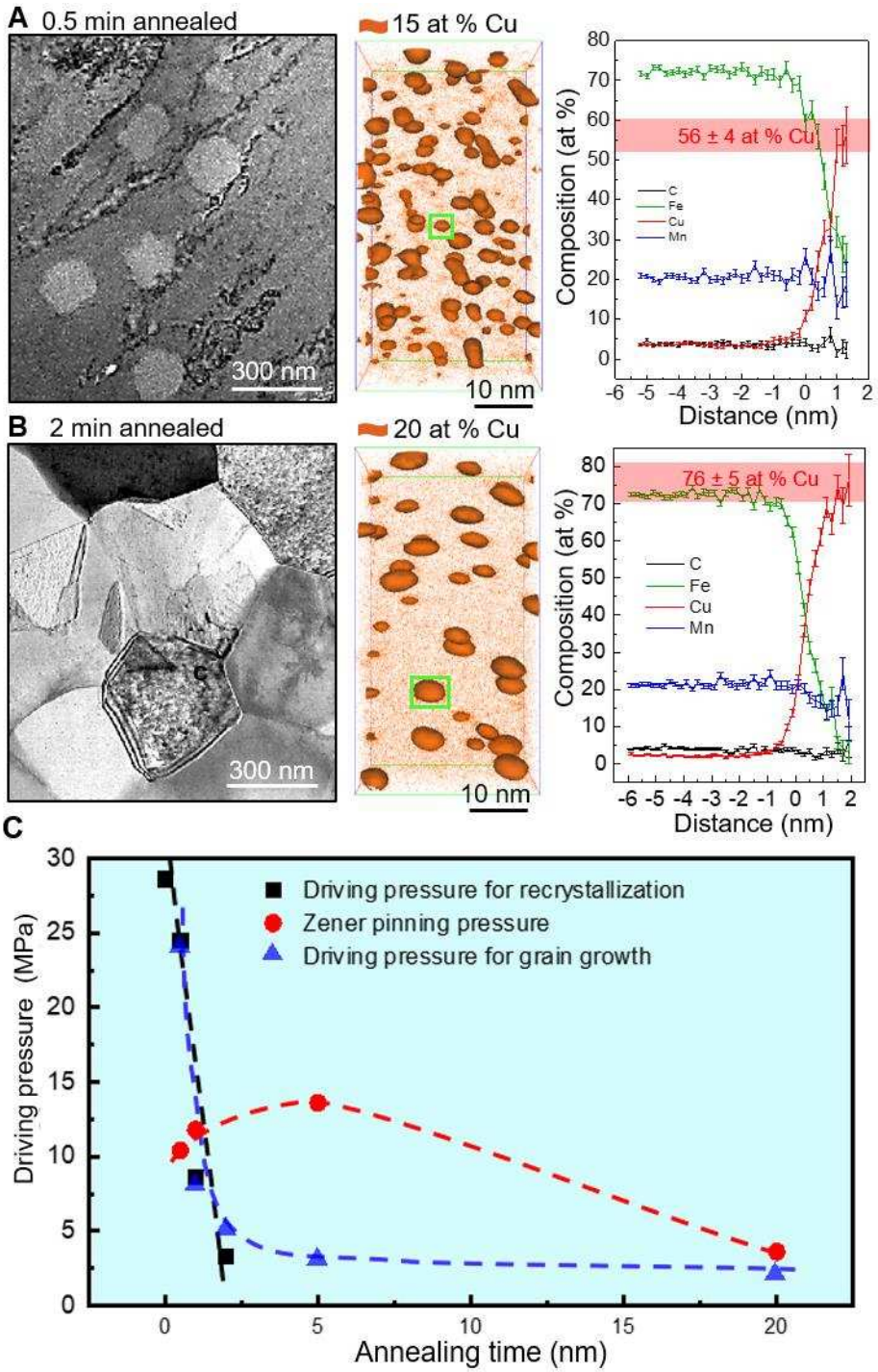
A 0.5 min annealed
300 nm
15 at % Cu
10 nm
56 ± 4 at % Cu
Composition (at %)
Distance (nm)
C
Fe
Cu
Mn
B 2 min annealed
300 nm
20 at % Cu
10 nm
76 ± 5 at % Cu
C
Driving pressure for recrystallization
Zener pinning pressure
Driving pressure for grain growth
Driving pressure (MPa)
Annealing time (nm)

2

3

Fig.4 (continue)

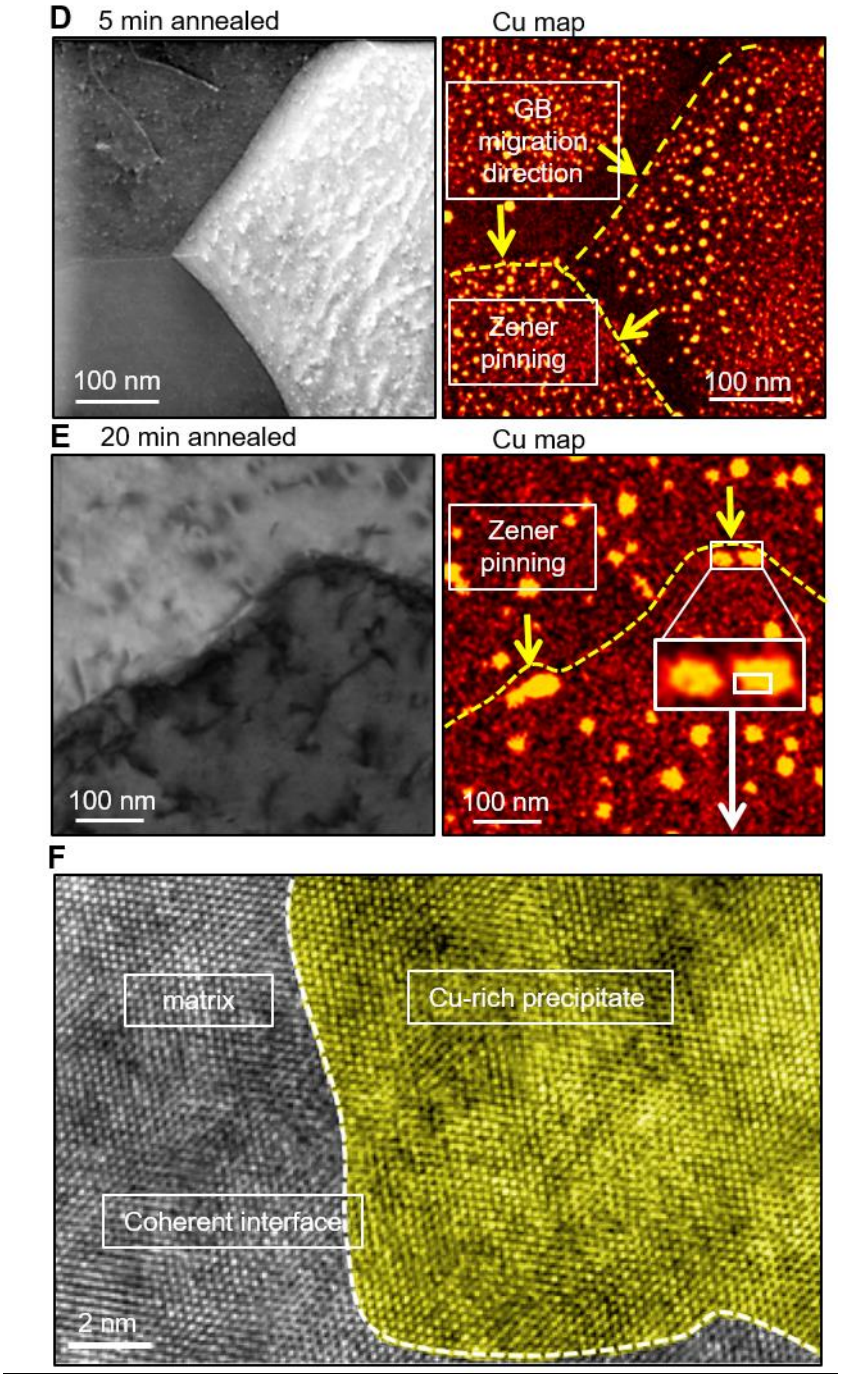

Figure 4 Mechanisms for effective grain refinement and high thermal stability. (**A**), (**B**), ABF-STEM images and atom probe analysis of 4Cu alloys showing the nucleation of recrystallization, formation of high-density Cu-rich nanoprecipitates and equiaxed UFG grains after annealing at 760 ℃ for 0.5 and 2 min, respectively. Precipitates grew with annealing time and accordingly the Cu content in the precipitates increases. (**C**), Evolution of driving pressure

for recrystallization, driving pressure for grain growth and Zener pinning pressure as a function of annealing time. (**D**), (**E**), ABF-STEM images and their corresponding STEM EDS-SI images of 4Cu alloys annealed at 760 ℃ for 5 and 20 min, respectively, demonstrating the evidence of Zener pinning. **f,** HRTEM image of one nanoprecipitate at a curved grain boundary (marked by a white rectangle in (E)) showing a coherent interface with the shrinking grain. The error bars are standard deviations of the mean. The isoconcentration surfaces in (A)and (B) are 15 at % and 20 at % Cu, respectively.

1 **Fig.5**

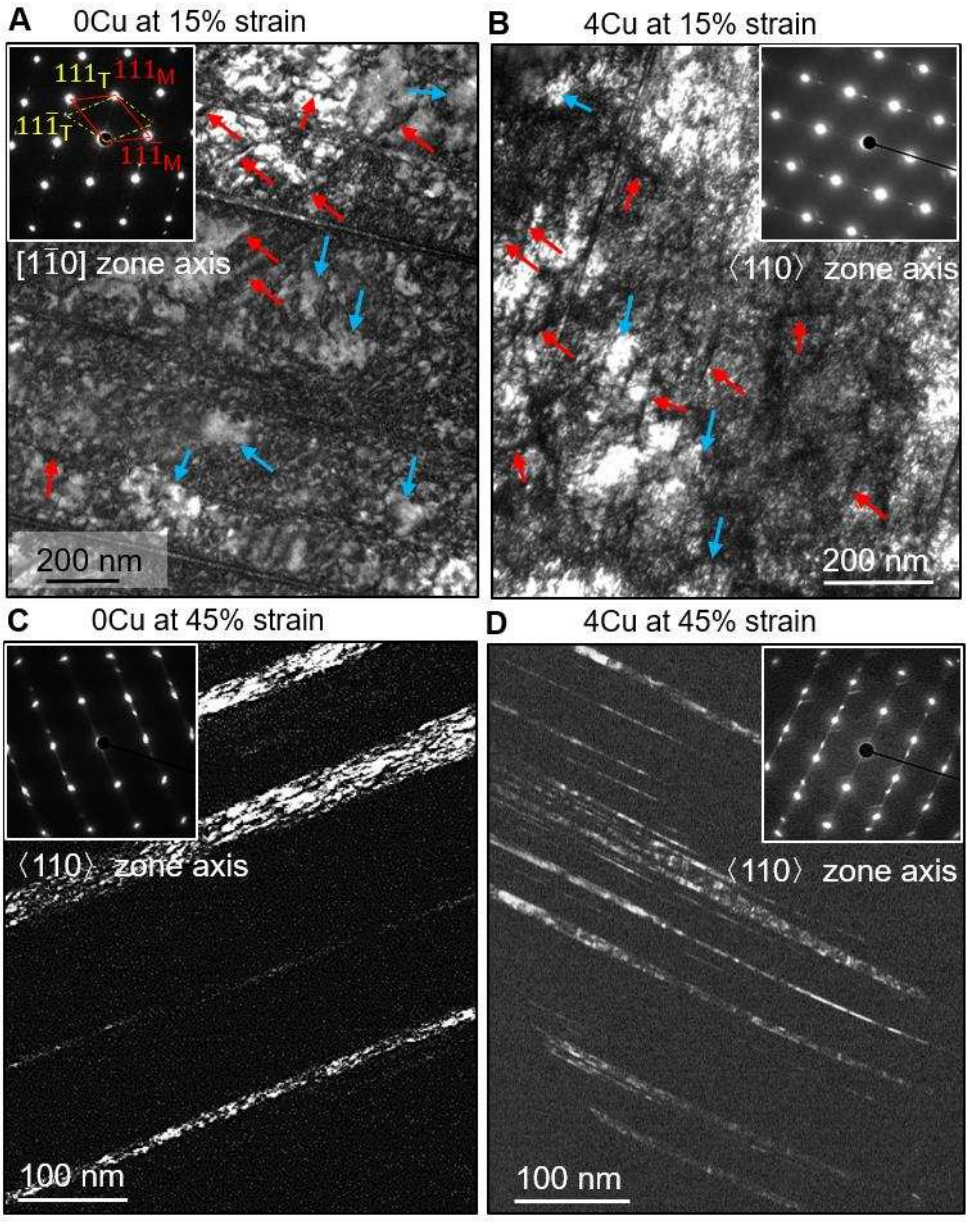
A
0Cu at 15% strain
111_T 111_M
$11\bar{1}_T$
$\bar{1}\bar{1}1_M$
[1$\bar{1}$0] zone axis
200 nm
B
4Cu at 15% strain
〈110〉 zone axis
200 nm
C
0Cu at 45% strain
〈110〉 zone axis
100 nm
D
4Cu at 45% strain
〈110〉 zone axis
100 nm

2

3

Fig.5 (continue)

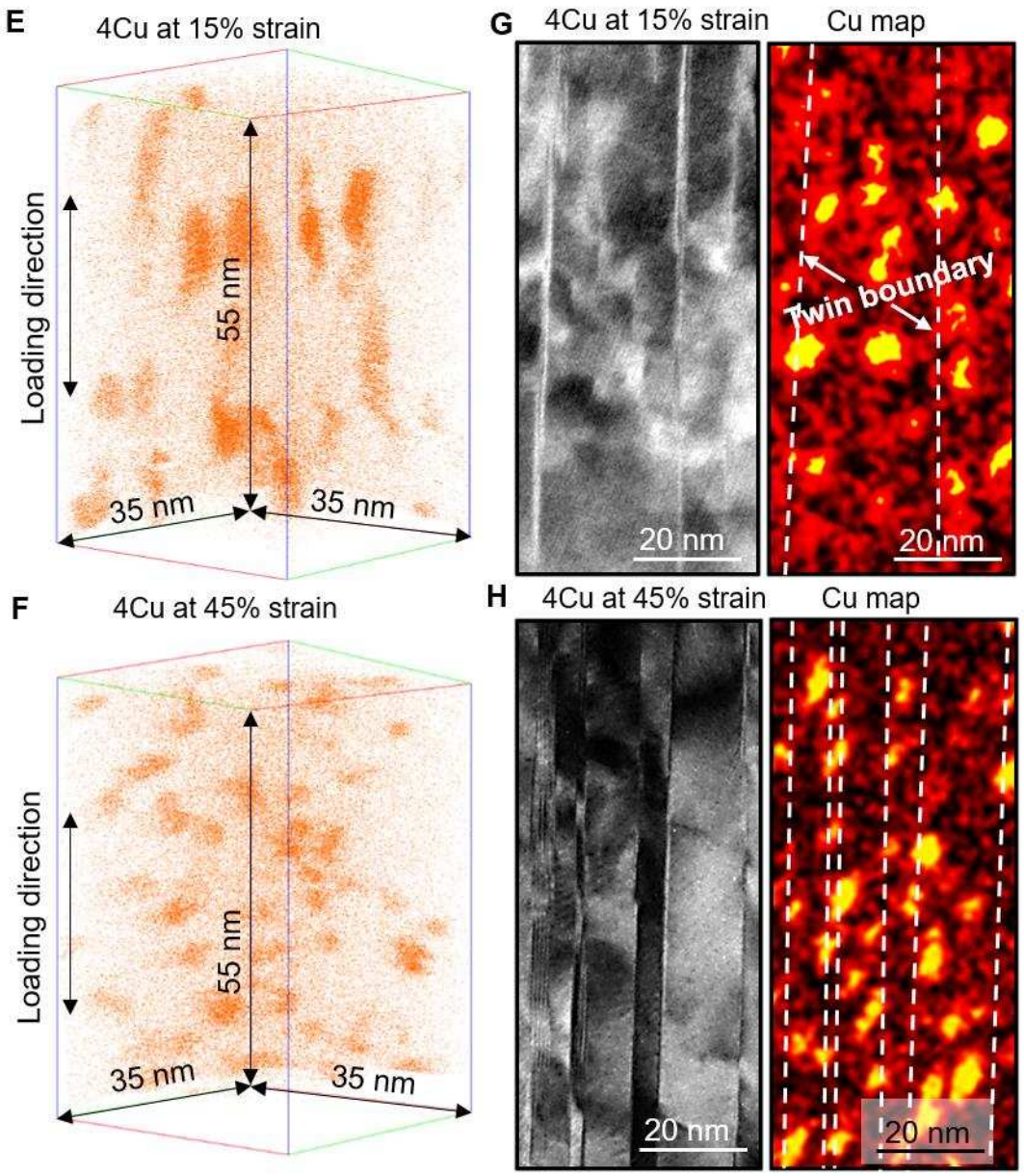

Fig.5. Deformed microstructure of UFG 0Cu and 4Cu alloys.(A), (B), Bight-field TEM images of UFG 0Cu and 4Cu alloys pre-strained to 15 %, respectively. Dense dislocation walls (marked by red arrows), dislocation cells (marked by blue arrows) and nanotwins were observed in both alloys. (C), (D), Dark-field TEM images of 0Cu and 4Cu alloys pre-strained to 45 %, showing thinner (7.9 ± 5.4 nm) and denser (with interspacing of 15.2 ± 14.3 nm) nanotwins in 4Cu alloys. (E)to (H), APT reconstructions and ADF-STEM images with the

corresponding STEM EDS-SI images of 4Cu alloys pre-strained to 15 % and 45 %, respectively. At the 15 % strain, part of Cu-rich precipitates was flattened along the loading direction and cut by nanotwins. At the 45 % strain, finer and denser Cu-rich precipitates were observed in 4Cu alloy, with more nanotwins cutting through nanoprecipitates.